Volume 19
Number 26
14 July 2023
Pages 4811–5030

Soft Matter

rsc.li/soft-matter-journal

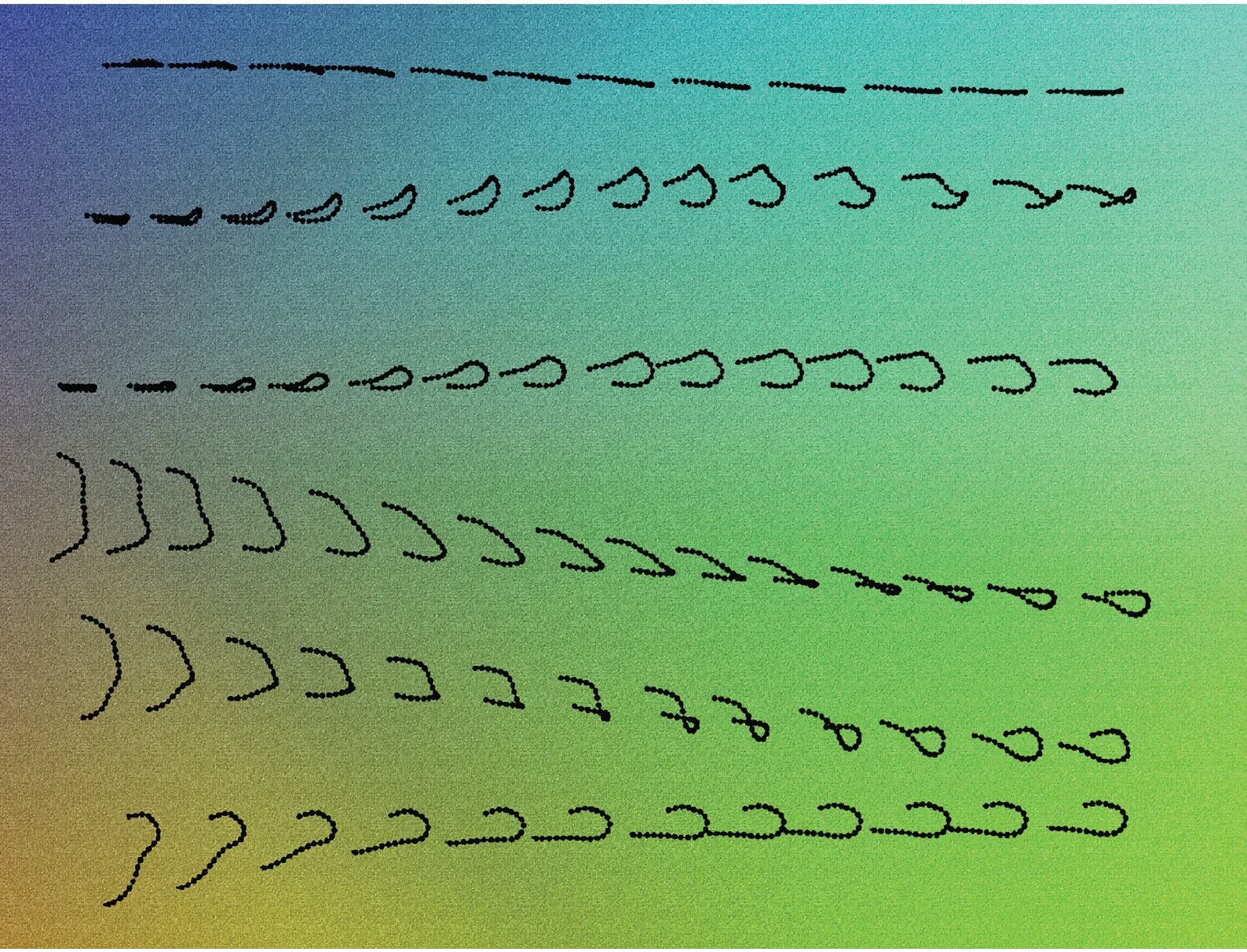

ISSN 1744-6848

ROYAL SOCIETY OF CHEMISTRY

PAPER
Maria L. Ekiel-Jeżewska *et al.*
Dynamics of ball chains and highly elastic fibres settling under gravity in a viscous fluid

Soft Matter

PAPER

Cite this: *Soft Matter*, 2023, **19**, 4829

Dynamics of ball chains and highly elastic fibres settling under gravity in a viscous fluid†

H. J. Shashank, Yevgen Melikhov and Maria L. Ekiel-Jeżewska *

Received 28th February 2023,
Accepted 16th May 2023

DOI: 10.1039/d3sm00255a

rsc.li/soft-matter-journal

We study experimentally the dynamics of one and two ball chains settling under gravity in a highly viscous silicon oil at a Reynolds number much smaller than unity. We record the motion and shape deformation using two cameras. We demonstrate that single ball chains in most cases do not tend to be planar and often rotate, not keeping the ends at the same horizontal level. Shorter ball chains usually form shapes resembling distorted U. Longer ones in the early stage of the evolution form a shape resembling distorted W, and later deform non-symmetrically and significantly out of a plane. The typical evolution of shapes observed in our experiments with single ball chains is reproduced in our numerical simulations of a single elastic filament. In the computations, the filament is modelled as a chain of beads. Consecutive beads are connected by springs. Additional springs link consecutive pairs of beads. Elastic forces are assumed to be much smaller than gravity. As a result, the fibre is very flexible. We assume that the fluid sticks to the surfaces of the beads. We perform multipole expansion of the Stokes equations, with a lubrication correction. This method is implemented in the precise HYDROMULTIPOLE numerical codes. In our experiments, two ball chains, initially one above the other, later move away or approach each other, for a larger or smaller initial distance, respectively.

1 Introduction

Recently, there has been a lot of interest in studying the motion of flexible and rigid microfibres under external forces[1] or ambient flows.[2,3] This research is guided by many potential applications in biological systems,[4–7] medical diagnostic techniques[8] or the design of new materials.[9,10]

In particular, it is important to study the gravitational settling of deformable microorganisms[11,12] and flexible micro-objects produced by innovative modern technologies.[13] Sedimentation of single or multiple deformable objects of different shapes has been investigated for a wide range of bending stiffness,[14–17] and also for non-negligible inertia effects.[18]

Dynamics of one, two, or three elastic fibres settling under gravity in a viscous fluid at a Reynolds number much smaller than unity have been extensively investigated theoretically and numerically.[14,15,19–27] Different types of motion and shape deformations have been found, depending on the values of the so-called elasto-gravitational number B, equal to the ratio of gravitational to elastic forces. Dependence on the initial relative orientations and relative positions of the fibres has been investigated.

Institute of Fundamental Technological Research, Polish Academy of Sciences, ul. Pawińskiego 5B, 02-106 Warsaw, Poland. E-mail: mekiel@ippt.pan.pl

† Electronic supplementary information (ESI) available: Videos. See DOI: https://doi.org/10.1039/d3sm00255a

However, to the best of our knowledge, experimental studies of sedimenting flexible fibres have been limited to rather short and moderately elastic fibres that tend to reach a stable, stationary, "V" or "U" shaped configuration.[25]

Therefore, the main goal of this paper is to explore experimentally the dynamics and the shape evolution of very flexible elongated objects that settle under gravity in a viscous fluid at a low Reynolds number. We searched for a very flexible object that could be used in experiments and would mimic a highly elastic fibre. After performing various tests, we decided to focus on ball chains. The ball chains are chains of identical beads. The beads are hollow inside. The ends of a dumbbell are located inside consecutive beads. There is a slack between the middle part of a dumbbell and the edges of the holes in beads. The beads can rotate around each other, with a certain upper limit for a bending angle.

The choice of ball chains was motivated by previous experiments with loops made of ball chains.[28] A comparison of the results of these experiments with numerical simulations of highly elastic rings was done in ref. 28 and indicated a qualitative agreement between the dynamics of these two flexible objects. The reason for this agreement is that ball chains are not fully flexible. Triplets of beads in a ball chain cannot bend more than a certain critical bending angle. Therefore, we expected that ball chains with open ends would also be a good model for a highly elastic fibre with open ends.

In this paper, we investigate the dynamics of a single ball chain or two ball chains one above the other. It is expected[29]

that the ball chain dynamics are similar to those of elastic filaments, if the ratio of elastic to gravitational forces is small enough. We also perform numerical simulations of a single sedimenting elastic filament. Our main goal is to investigate how a planar vertical symmetric U-shape, inherent in the dynamics of moderately flexible filaments, becomes unstable as the flexibility is increased. We also compare our findings with the dynamics predicted numerically for very flexible elastic filaments in ref. 14.

The paper is structured as follows. In Section 2, we present the experimental setup, materials, and methods used, including the image processing techniques. Section 3 and the Supplementary videos (ESI†) contain the experimental results – an evolution of the shapes and positions of a single ball chain and of a pair of ball chains one above the other. In Section 4, we describe a theoretical model and present numerical results for a single elastic filament. The numerical results agree with the experiments. In Section 5 we argue why the two close fibres decrease their distance with time. Finally, we conclude in Section 6.

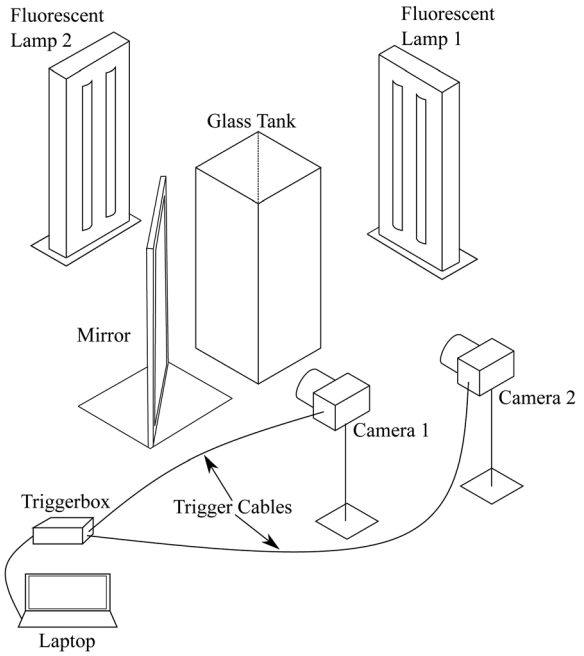

Fig. 1 Schematic of the experimental arrangement.

2 Experimental techniques, materials and methods

2.1 Experimental arrangement

We conduct experiments within a glass tank of inner dimensions 200 mm width, 200 mm depth and 500 mm height, that is filled with highly viscous silicon oil (manufactured by Silikony Polskie) with kinematic viscosity $\nu = 5 \times 10^{-3}$ m^2 s^{-1} and density $\rho = 970$ kg m^{-3} at 25 °C. Into this tank, we drop flexible ball chains.

The motion of the ball chains is viewed using two cameras placed in perpendicular orientations, corresponding to the front and side views, as shown in the schematic of the experimental setup in Fig. 1. Camera 2 views the glass tank directly, while camera 1 views the glass tank *via* a first surface mirror (manufactured by First Surface Mirror LLC, USA) placed at an angle of 45°. These two views provide greater insight into the lateral movements of the ball chains. A fluorescent lamp is placed behind each of the vertical faces of the tank opposite where the cameras are located. Camera 1 is illuminated by fluorescent lamp 1, through the mirror, and camera 2 is illuminated by fluorescent lamp 2, as seen in the schematic shown in Fig. 1. This arrangement of the lamps ensures the best illumination of the tank, with the opaque sedimenting ball chains being clearly contrasted with the bright background.

The cameras used are two identical full-frame DSLRs (Canon 5D Mark IV) with a resolution of 30 megapixels and equipped with a 100 mm prime lens. Both cameras are triggered externally so that photographs can be captured at the same time. We use an Esper Triggerbox to trigger both cameras simultaneously. The trigger box maintains a trigger delay of less than 20 ms between the two cameras. The trigger box itself is controlled by a laptop, and the photographs are captured at the maximum permissible rate allowed by the DSLR cameras (1 photo per second). The exposure time of the photographs from both cameras is set to 1/125 s to ensure that the motion of the ball chains remains frozen for the entire duration of the exposure time. The distance travelled by the ball chains at this time is smaller than a pixel. The *f*-number is set to its highest available, *f*/32 (*i.e.* the smallest aperture), to ensure that the ball chains remain in focus even as they meander out of the focal plane of the cameras. Finally, the ISO rating is kept at 400 to ensure sufficient image brightness, whilst also ensuring low to moderate noise levels.

The cameras are placed in portrait orientation at about 800 mm from the front faces of the glass tank, according to their respective views. This gives a field of view of about 300 mm in the vertical direction and 200 mm in the horizontal direction. We centre the cameras at the middle of the glass tank so that approximately 100 mm from the free surface and 100 mm from the bottom glass face are absent in the photographs, thereby reducing the effect of the free surface and the bottom glass wall on the sedimenting ball chains.

2.2 Ball chains

The ball chains that are used in this work (manufactured by Koniarscy S.C., product no. LL01114AS) consist of metallic beads. The beads are hollow inside. There is a central hole drilled through each metallic bead. The beads are connected in series by metallic rigid dumbbells running through the holes, as illustrated in Fig. 2. There is slack between the middle part of the dumbbell and the edges of the hole in a bead. As a result, the distance between consecutive beads can change. Also, the beads are able to bend around each other, with the bending angle limited by the dumbbell length.

The diameter of all metallic beads is the same, $d = 1.5$ mm, and ball chains of different lengths (*i.e.*, different numbers of

Fig. 2 A ball chain used in the experiments and a metallic dumbbell connecting consecutive metallic beads of the chain.

beads N) have been used, typically with $N = 12$ and $N = 20$. The 'average' filament length L is defined as $L = d + (N - 1)d_d$, where d_d is the average distance between the bead centres. In our experiments, $d_d \approx 1.8$ mm.

The ball chains are denser than silicon oil and settle down owing to gravity. Hydrodynamic interactions between the beads cause the whole ball chain to bend while moving. The ball chains do not have an inherent elasticity, and this allows them to bend with zero spending of energy. Bending angle β_i of a triplet of consecutive beads, $i - 1$, i and $i + 1$, is defined by the relationship

$$\cos\beta_i = \frac{(\boldsymbol{r}_i - \boldsymbol{r}_{i-1}) \cdot (\boldsymbol{r}_{i+1} - \boldsymbol{r}_i)}{|\boldsymbol{r}_i - \boldsymbol{r}_{i-1}||\boldsymbol{r}_{i+1} - \boldsymbol{r}_i|}, \quad (1)$$

where $\boldsymbol{r}_i = (x_i, y_i, z_i)$ is the position of the centre of the bead i (see Fig. 3).

The change of a ball-chain shape is limited by: (a) the maximum bending angle of a bead triplet, and (b) the number of beads in the ball chain. Naturally, a ball chain that allows a larger bending angle of a bead triplet would allow for larger bending of the whole ball chain. Furthermore, for a larger number of beads in the ball chain the shape can be more bent, too. We have measured the bending angles of bead triplets of the sedimenting ball chains, as well as when the ball chain is outside the fluid. In the latter case, we find that the maximum bending angle β_i of a bead triplet is 55° when we force the ball chain to bend to its maximum possible extent. On the other hand, the maximum bending angle of a bead triplet of a sedimenting ball chain ranges from 33° to 40° indicating that the ball chain does not bend to its full extent as it sediments in our experiments.

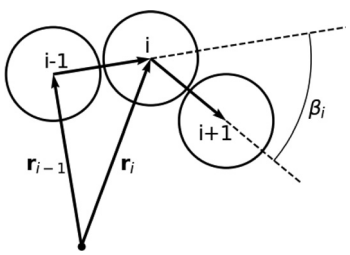

Fig. 3 Schematic of a section of a ball chain. A local bending angle β_i is shown.

In this paper, we will study sedimentation of a single type of ball chain, thus ensuring that the ball chain's maximum deformation is a function of the number of beads alone. We will first investigate time-dependent shape and velocity of a single ball chain settling under gravity in the silicon oil. We will then present the interaction between two ball chains that sediment one above the other but do not touch.

2.3 Experimental methods & analysis

The experiments are conducted by manually dropping one or two ball chains approximately at the centre of the tank, in an approximately horizontal orientation. A single ball chain is always inserted parallel to the plane of view of camera 2. The experiments with two sedimenting ball chains are performed by placing the ball chains one by one, at a small time separation, resulting in the position of one above the other in a perpendicular orientation. The ball chain placed earlier (the bottom one) is located parallel to the plane of view of camera 2 (perpendicular to the plane of view of camera 1) and the ball chain placed later (the top one) is located parallel to the plane of view of camera 1 (perpendicular to the plane of view of camera 2). The cameras are triggered at the moment when both ball chains are already inside the tank, and photographs are acquired until the top ball chain exits the field of view. We stress that, given the pliable nature of the ball chains, it is not possible to ensure that the ball chains are always exactly horizontal nor exactly straight once they are inserted. Moreover, the ball chains bend transversely just after entering the fluid, and they are already significantly curved when they enter the camera field of view.

We analyse the motion of the ball chains by extracting relevant data from the photographic image sequence obtained from both cameras. The recorded photographs from each camera are imported into MATLAB, and image processing techniques are applied to identify each of the ball chains. The post-processing steps involve image thresholding, image binarisation, noise removal and filling small gaps in the binary objects caused by shadows or reflections. Following these steps, each ball chain is uniquely identified in each frame and in each camera view. Once the ball chains are uniquely identified, we then calculate the various parameters of the ball chains to better understand their sedimentation mechanics. Some of the characteristic parameters are illustrated in Fig. 4.

(i) Following ref. 15 and 20, we determine the bending amplitude A as the absolute difference between the uppermost location y_{top} and the lowermost location y_{bot} of the ball chain, $A = |y_{top} - y_{bot}|$, and we divide it by the filament length L (defined in the previous section).

(ii) We also evaluate the vertical component v_y of a ball chain time-dependent velocity as the ratio of the vertical distance between its lowermost locations at the times of the two consecutive photographs (approximately equal to the distance travelled by the ball chain between two consecutive photographs) to the

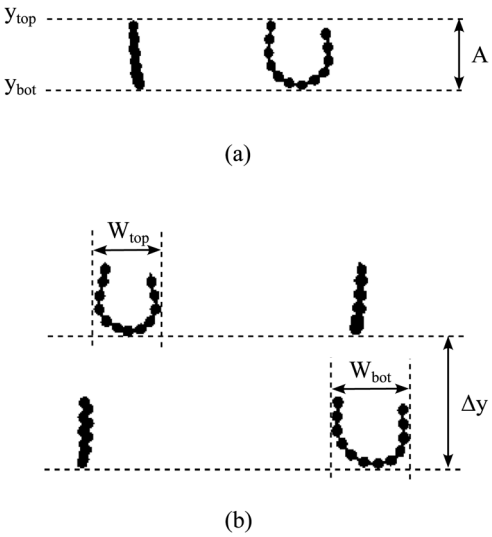

Fig. 4 Schematic describing the definition of parameters. (a) Bending amplitude A, determined in single and multiple ball chain experiments. (b) Vertical distance Δy between two ball chains and their widths W.

time difference between those photographs, $v_y = (y_{bot}^{t+\Delta t} - y_{bot}^{t})/\Delta t$, with $\Delta t = 1$ s. These quantities are first calculated separately from each camera view and are later averaged across the two views.

The fluid and the ball chains are chosen in such a way that a typical Reynolds number in the experiments is much smaller than unity, with $\mathrm{Re} = 7 \times 10^{-4}$–$10^{-3}$ if based on the ball chain width, and $\mathrm{Re} = 8 \times 10^{-3}$–$2 \times 10^{-2}$ if based on the ball chain length.

We will now discuss the uncertainty of the measurements. The accuracy in the calculation of A and v_y depends on the accuracy of the identification of y_{bot} and y_{top} during post-processing. The high contrast between the back-lit image of the ball chains and the bright background ensure that the errors in identifying the edges are minimal. The error of y_{bot} and y_{top} is around ± 0.1 mm (± 2 pixels), which leads to the bending amplitude A having an uncertainty of ± 0.15 mm, and the vertical velocity v_y an uncertainty of ± 0.19 mm s^{-1}. This yields a measurement uncertainty of about 10% for a single camera measurement. Moreover, during the combined measurement with both cameras, the proximity of cameras to the glass tank, coupled with the tendency of the ball chains to drift off the focal plane of the cameras, may cause a systematic error due to parallax. The parallax errors are most noticeable at the extreme ends of the field of view, *i.e.*, at the top and bottom. However, the influence of parallax is not significant for the measurement of local quantities, such as the bending amplitude A and the local velocity v_y. Furthermore, the walls and the fluid free surface also affect the dynamics. Long-range hydrodynamic interactions of the ball chains with the walls slow down the motion and may influence their shapes, particularly if the ball chains drift away from the centre of the tank.

3 Experimental results

3.1 Sedimentation of a single ball chain

We recorded and analysed the sedimentation of a single ball chain in 5 experimental trials for 12-bead ball chains and in 14 experimental trials for 20-bead ball chains. (The shorter ball chains did not show rich dynamics in contrast to the longer ones, hence the moderate difference in the number of experimental trials.) Snapshots from three trials for each type of the ball chains are shown in Fig. 5 and 6, respectively, with the time interval between consecutive snapshots being 10 s.

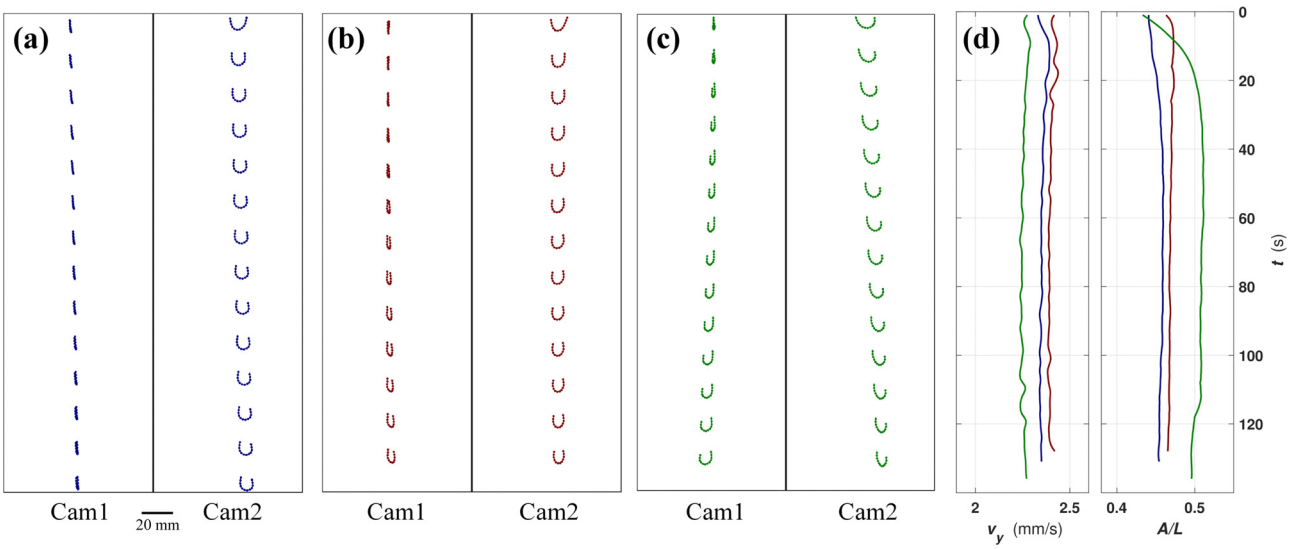

Fig. 5 Snapshots of a single 12-bead ball chain ($L \approx 21.3$ mm) settling under gravity in a viscous oil, taken simultaneously by two cameras (Cam1 and Cam2) located at the same level, and with perpendicular lines of sight: (a) a trial without rotation; (b) a trial with rotation; (c) a trial with rotation and non-horizontal orientation of the end-to-end vector; (d) the sedimentation velocity v_y and the bending amplitude A/L *vs.* time t, plotted with blue, red, and green lines for the trials shown in (a), (b), and (c), respectively. Experimental movies that correspond to the trials (a), (b), and (c) are shown in the ESI† in Videos 5a, 5b and 5c, respectively.

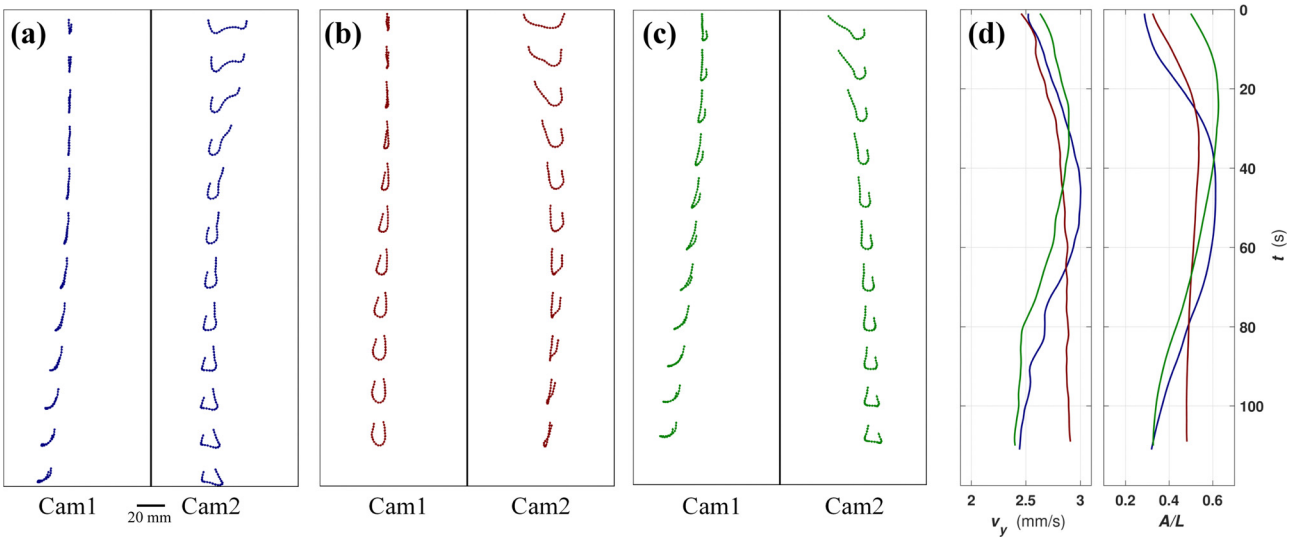

Fig. 6 Snapshots of a single 20-bead ball chain ($L \approx 35.7$ mm) settling under gravity in a viscous oil, taken simultaneously by two cameras (Cam1 and Cam2) located at the same level, and with perpendicular lines of sight: (a) a trial that begins with a W-shape; (b) a trial that begins with a U-shape; (c) a trial that begins with an asymmetric hook-shape; (d) the sedimentation velocity v_y and the bending amplitude A/L *vs.* time, plotted with blue, red and green lines for the trials shown in (a), (b) and (c), respectively. Experimental movies that correspond to the trials (a), (b) and (c) are shown in the ESI† in Videos 6a, 6b and 6c, respectively.

The difference in shapes between the 12 and 20-bead ball chains is evident from the snapshots. In each figure, we present three different trials that show distinct sedimentation dynamics. In addition to the snapshots, the evolution is quantified by the plots of the time-dependent vertical velocity v_y and bending amplitude A/L for the runs shown in the snapshots.

A typical evolution of the 12-bead ball chain is illustrated in Fig. 5 and Videos 5a–c (ESI†). The ball chain consistently shows a slightly distorted U-shape during all the trials. In Fig. 5(a), it seems that the ball chain remains close to a plane, similar to the previous numerical and experimental studies of relatively short elastic fibres of moderate stiffness.[14,15,20–26]

The existence of a stable stationary U-shaped vertical configuration of an elastic filament was predicted numerically, provided that the bending stiffness is above a certain threshold value,[14,15,20,23,24,26] and was confirmed experimentally.[25] Dynamics of ball chains have not been studied numerically so far, but it could be expected that they are similar to the dynamics of highly elastic fibres. Our experimental results indicate that shorter ball chains indeed tend toward a certain bent U-shape, with some small deviations. For example, in Fig. 5(a), the fibre is almost planar, and this plane is slightly inclined with respect to vertical, and a small sideways drift is observed, as predicted by numerical simulations of moderately elastic filaments performed in ref. 14, and illustrated in the middle panel of their Fig. 1.

We also observe behaviour that has not been reported in previous studies of elastic fibres. In Fig. 5(b), the ball chain rotates around the gravity direction in a screw-like fashion as it sediments. Previous studies have shown the screw-like rotation of an elastic fibre when under the influence of a second fibre,[14] but not in the case of a fibre sedimenting alone. The rotation is caused by small deviations from a planar vertical shape, such that the rotational–translational mobility is different from zero.

In Fig. 5(c), one can also see, in addition to the screw-like rotation, that the shape clearly has no left-right symmetry, and the endpoints of the ball chain are not horizontally aligned. For some of the trials, like those shown in Fig. 5(a) and (c), the deviation from the horizontal orientation of the end-to-end vector increases with time, contrary to the expectations that a flexible relatively short filament would tend toward a stable configuration with the left-right symmetry. Such an attracting symmetric configuration was found numerically for relatively stiffer elastic fibres.[14,15,20–22,26] For moderate stiffness, out-of-plane shapes found in ref. 14 also exhibit left-right symmetry.

The difference between the dynamics observed in Fig. 5(a)–(c) is likely due to the difference between the initial configurations when the ball chains are inserted into the fluid. However, it is worth noting that the small differences in shapes, observed in Fig. 5(a)–(c), result in the comparable vertical velocity of sedimentation v_y and the bending amplitude A/L, shown in Fig. 5(d) (the differences are not greater than 10%). In other words, the velocity of the ball chain exhibiting rotation and a clear lack of left-right symmetry, with the pronounced end-to-end asymmetry, shown in Fig. 5(c), is very close to that of the ball chain exhibiting only rotation and almost no end-to-end asymmetry, as seen in Fig. 5(b).

The common feature of the dynamics of the shorter ball chains is the lack of a uniquely defined stable configuration reached at a relatively short time of the evolution. Rotation and breaking of the left-right symmetry seem to be typical.

The 20-bead ball chains exhibit a distinctly wider range of different shapes than the 12-bead ball chains, as seen in Fig. 6 and Videos 6a–c (ESI†). We notice, unlike in the 12-bead runs,

that the first observed shape of 20-bead ball chains is different in each run. From the point of view of camera 2, we see that the shape of the ball chain as it enters the field of view is: a bimodal W-shape, as in Fig. 6(a); a wide U-shape, as in Fig. 6(b); an asymmetric, hook-shape, as in Fig. 6(c). The initial shapes in Fig. 6(a) and (b) are slightly asymmetric, but the initial shape in Fig. 6(c) significantly breaks the left-right symmetry.

Fig. 6 illustrates that ball chain trajectories and the evolution of their shapes are sensitive to the initial configuration. The perturbed bimodal W-shapes, observed as the first snapshots, deform with time, in agreement with the numerically observed instability of the W-shape of highly elastic, relatively long filaments, reported in ref. 20. Hence, in Fig. 6(a), the initial W-shape evolves into the hook-shape before bending out of the plane and drifting away from the centre of the tank. On the other hand, in Fig. 6(c), the ball chain is already at the hook-shape phase as it enters the field of view, and continues to bend out of a plane and drift away from the centre of the tank. These two runs can thus be said to be similar to each other, but ''shifted in time'' with respect to each other.

The first shape observed in Fig. 6(b) resembles a deformed U-shape rather than a deformed W-shape, and it changes in time differently from Fig. 6(a) and (c), but a bit similar to the evolution of the 12-bead ball chain, shown in Fig. 5(b). However, the observed shapes are significantly non-planar and with a pronounced asymmetry, in contrast to the shorter ball chains. Moreover, they do not seem to converge to a stable planar and symmetric U-shape. This seems to be in agreement with the non-existence of a stable stationary configuration for sufficiently elastic filaments.[14,15,20]

The stark ranges in the first ball-chain shapes in Fig. 6 (W-shape, U-shape and hook-shape) indicate that the shapes are sensitive to the initial configuration. It is thus tempting to attribute this variation to the uncertainty of keeping the ball chains horizontal and straight as they are inserted into the tank. We have observed runs that, for instance, exhibit the hook-shape, but do not exhibit the significant out-of-plane bending, which can be related to only a small initial perturbation of the planar shape. It might be possible that the out-of-plane bending would have eventually been observed if the tank was higher, and a small unstable perturbation had enough time to grow. The behaviour of the 20-bead ball chains is thus complex, and it is difficult to classify it, as it was possible for the 12-bead ball chains. It is remarkable that our observation of the subsequent W, hook, and out-of-plane bending agrees qualitatively with the trajectory observed in previous numerical studies of highly elastic (semi-flexible) fibres at large bending amplitudes, shown in the right panel of Fig. 1 in ref. 14. Even though our experimental observations of the trajectory span only a part of the time of the numerical simulation, the agreement is striking.

The plots of the vertical sedimentation velocity v_y and the bending amplitude A for our experiments, shown in Fig. 6(a)–(c), are presented in Fig. 6(d). A correlation between both parameters is visible. As A increases, so too does v_y, and a reduction in A leads to a reduction in v_y. The effect of the dynamic variation of the shape of the ball chains on the vertical sedimentation velocity is evident from these snapshots, resulting in similar curves of A and v_y.‡ The correlation of the maxima for longer fibres is related to the formation of hook-shapes. In this case, the width of the bent fibre is small, and the hydrodynamic drag is small, too. For shorter fibres this correlation is not evident, see, *e.g.*, the green curves in Fig. 5(d). In this case, a large bending amplitude corresponds to a wide shape, large hydrodynamic drag, and small velocity.

3.2 Sedimentation of two interacting ball chains

3.2.1 Experimental observations. In order to study the hydrodynamic interactions of two ball chains as they settle under gravity in a viscous fluid, the ball chains are inserted horizontally one above the other, such that their centres are aligned vertically, with the bottom ball chain being in the focal plane of camera 1 (and perpendicular to camera 2) and the top ball chain being in the focal plane of camera 2 (and perpendicular to camera 1). The ball chains are inserted manually, one by one, at the centre of the tank. The motion of both ball chains is recorded using the camera arrangement shown in Fig. 1. We performed a number of trials, *i.e.*, 13 trials for the 12-bead ball chains and 23 trials for the 20-bead ball chains, to study time-dependent configurations of the sedimenting ball chains.

We present the typical behaviour of a pair of ball chains in Fig. 7 and Videos 7a, c and Fig. 8 and Videos 8a, c (ESI†) for the 12-bead and 20-bead ball chains, respectively. In both Fig. 7 and 8, we present two individual trials, shown in panels (a), (b) and (c), (d), respectively. In addition to the snapshots visible in panels (a) and (c), we also show in panels (b) and (d) the corresponding bending amplitudes A and the sedimentation velocities v_y of the top and bottom fibres.

In Fig. 7(a), we observe that the 12-bead ball chains approach each other as they sediment (the term ''attraction'' is used to describe such a behaviour). It is shown in Fig. 7(b), that the top ball chain (coloured blue) exhibits a larger bending amplitude, as well as a higher sedimentation velocity than the bottom ball chain (coloured red). In other words, the top ball chain bends in such a way that its mobility is larger than the mobility of the bottom ball chain.

Previous studies of elastic and semiflexible fibres have also demonstrated the attraction between two fibres of low/moderate elasticity that are one above the other.[14,30] In our experiments with the 12-bead ball chains, we have consistently observed that the attraction of the ball chains is correlated with the top ball chain having a larger bending amplitude than the bottom one. This finding is in agreement with the results of numerical simulations, shown in Fig. 5 in ref. 14, where $A_{\mathrm{top}} > A_{\mathrm{bot}}$. The attraction of elastic fibres settling one above the other was also found in numerical simulations presented in ref. 30.§

‡ For some of the trials with 20-bead ball chains, the correlation is not as evident, which is related to the more complex shapes of the ball chains.

§ Numerically determined shapes of elastic fibres sedimenting within the same vertical plane, presented in Fig. 2 in ref. 30, are different from those shown in Fig. 5 in ref. 14, probably owing to the use of a different, simplified theoretical model.

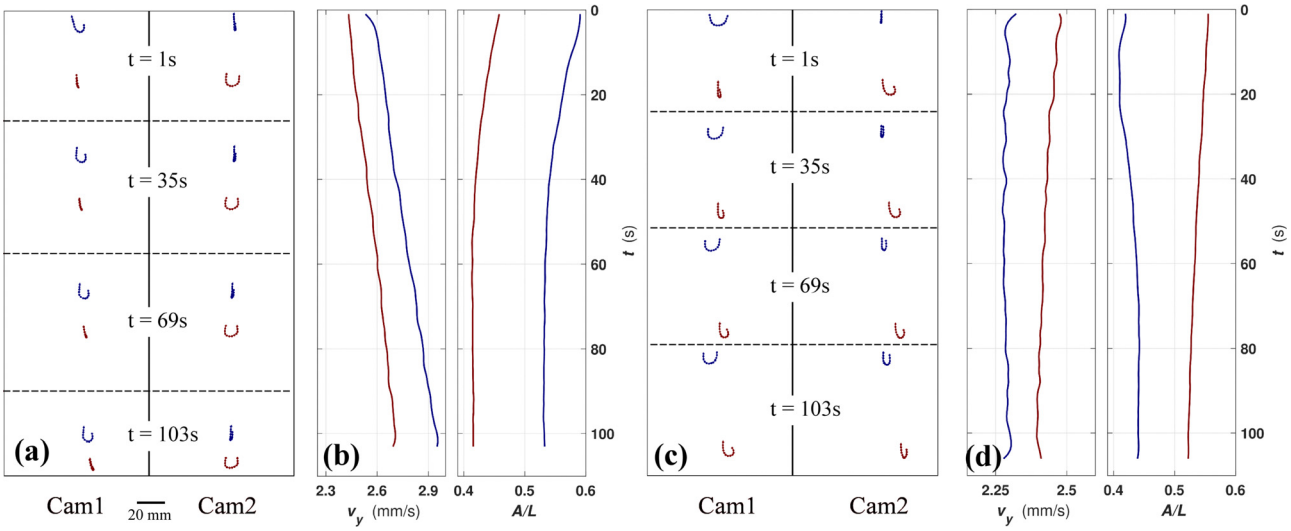

Fig. 7 Results of two experimental trials for a pair of 12-bead ball chains settling under gravity in a viscous oil, traced simultaneously by two cameras (Cam1 and Cam2) located at the same level, and with perpendicular lines of sight: (a) snapshots of a trial in which the ball chains come closer to each other; (c) snapshots of a trial in which the ball chains separate from each other; (b and d) the sedimentation velocity v_y and the bending amplitude A/L *vs.* time, plotted for the trials in (a and c), respectively. The blue colour represents the top ball chain while the red colour represents the bottom ball chain. Experimental movies that correspond to the trials shown in (a and c) are shown in the ESI† in Videos 7a and 7c, respectively.

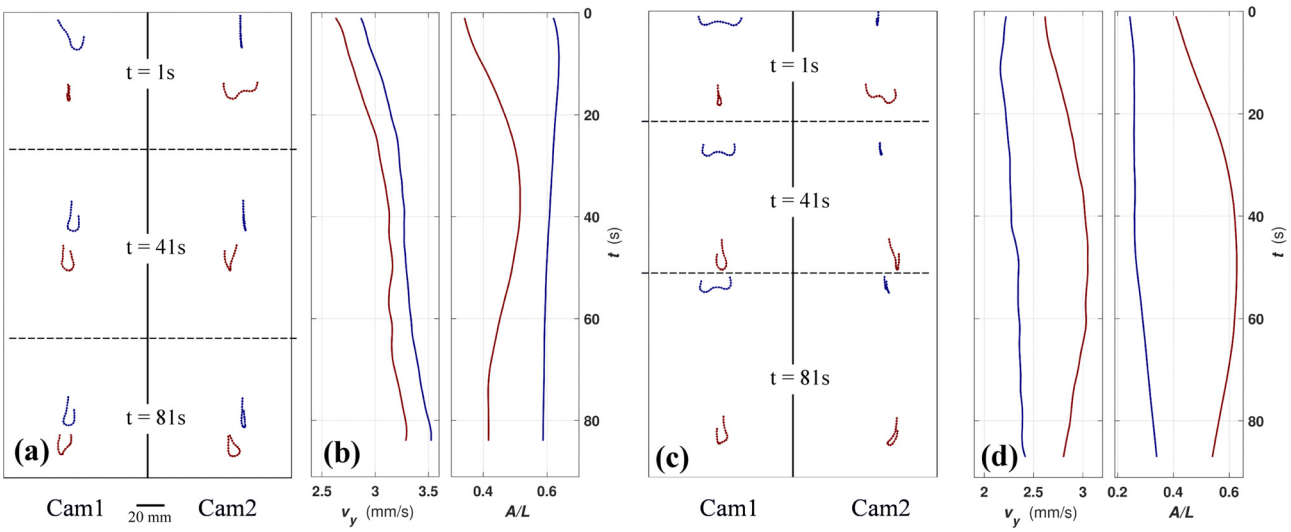

Fig. 8 Results of two experimental trials for a pair of 20-bead ball chains, settling under gravity in a viscous oil, traced simultaneously by two cameras (Cam1 and Cam2) located at the same level, and with perpendicular lines of sight: (a) snapshots of a trial in which the ball chains come closer to each other; (c) snapshots of a trial in which the ball chains separate from each other; (b and d) the sedimentation velocity v_y and the bending amplitude A/L *vs.* time, plotted for the trials in (a and c), respectively. The blue colour represents the top ball chain while the red colour represents the bottom ball chain. Experimental movies that correspond to the trials shown in (a and c) are shown in the ESI† in Videos 8a and 8c, respectively.

We have also observed that ball chains can move away from each other. This relative motion is called "repulsion". To the best of our knowledge, the repulsion of flexible elongated objects, located one above the other, has not been reported so far. An example of repulsion is clearly visible in the snapshots in Fig. 7(c). The bottom ball chain (coloured red) moves away from the top ball chain (coloured blue) as both ball chains sediment. The plots of sedimentation velocities v_y and bending amplitudes A of both fibres, presented in Fig. 7(d), corroborate the separation of the ball chains, with the bottom ball chain having a larger bending amplitude, and, consequently, a larger sedimentation velocity than the top ball chain.

In our experiments, the shapes of the ball chains typically do not have right-left symmetry, and the end-to-end line of a ball-chain usually is not horizontal. It seems that the larger these effects are, the larger is the settling speed. On the other hand, deviations from the horizontal location of the ball chain arms seem to be random, and for the top ball chain, they can be both smaller and larger than for the bottom one. We have not observed a tendency to approach with time symmetric or even

planar shapes, nor any specific relative orientation of the ball chains.

The 20-bead ball chains also exhibit the two distinct behaviours described for the 12-bead ball chains: vertical attraction or repulsion. Fig. 8(a) shows snapshots from a trial where the ball chains approach each other, while Fig. 8(c) shows snapshots from another trial where the ball chains move away from each other. In most runs, we observe a direct correlation between the bending amplitude A and the sedimentation velocity v_y – the larger the bending amplitude, the faster the sedimentation velocity (see Fig. 8(b) and (d)), but there are exceptions. If the top ball chain bends more than the bottom ball chain, the ball chains approach each other. If the bottom ball chain bends more than the top ball chain, the ball chains move away from each other.

3.2.2 How much do hydrodynamic interactions between two ball chains change the isolated ball chain dynamics? Previous studies on the dynamics of two highly elastic filaments in a top-down initial orientation suggest that at large values of B, the dynamics of the filaments are dominated by the behaviour of a single filament, and not by hydrodynamic interactions between the two filaments, if the distance between the filaments is not small.[14] The shapes exhibited by the separating 20-bead ball chains that are relatively far from each other in an experimental trial shown in Fig. 8(c) seem to agree with this assessment, since the sequence of the ball chain shapes is close to the different stages of their individual sedimentation process – for instance, both ball chains in the first frame of Fig. 8(c) are in the bimodal W-phase, but the bottom ball chain is already beginning to enter the hook-phase. This time shift could be easily understood since the upper ball chain was inserted into the fluid later than the lower one.

The velocity of a hook-shaped ball chain is larger than that of a W-shaped ball chain, as discussed earlier and shown in Fig. 6 of Section 3.1. Therefore, the sequence of shapes shown in Fig. 8(c) explains why the ball chains move away from each other. (However, the limited range of shapes exhibited by the 12-bead ball chains, shown in Fig. 7(c), makes it difficult to explain why they move away from each other.)

For the top and bottom ball chains relatively close to each other, it is expected that their mutual hydrodynamic interactions would cause them to approach each other,[14] as discussed in Section 5. We have seen clear evidence of an attracting behaviour of the hydrodynamic interactions in a few trials where the top ball chain, which is not directly above the bottom ball chain but still coming closer to the bottom ball chain changes its trajectory and turns towards the bottom ball chain once it is close enough (see Videos 7a and 8a in the ESI†). Direct evidence of hydrodynamic interactions can be found in Fig. 7(b) and 8(b) – we observe that both ball chains sediment at a larger velocity when compared to the sedimentation velocity of an isolated ball chain, shown in Fig. 5(d) and 6(d). It is well-known that a particle sedimenting close to other particles moves faster than in the absence of any other particles.

To further illustrate the relevance of hydrodynamic interactions at small distances, we present in Fig. 9 the time-dependence of vertical distance Δy between the two ball chains as they traverse the height of the tank, for all the experimental runs performed (see Fig. 4 for the definition of Δy). We adopt the following colour code in the plots: the runs with a greater vertical separation distance between the ball chains at the end of the run than at the beginning are assigned the colour green (moving away from each other, repelling), whereas the runs with a smaller vertical separation distance at the end of the run than at the beginning are assigned the colour red (approaching each other, attracting). In other words, the green curves correspond to runs in which $\Delta y_{t=\text{end}} > \Delta y_{t=0}$ and the red curves correspond to runs in which $\Delta y_{t=\text{end}} < \Delta y_{t=0}$.

It is clear from the plots in Fig. 9 that the red curves correspond to two ball chains that are closer to each other at the beginning of the run. We observe this tendency for both the 12-bead as well as the 20-bead runs. Hydrodynamic interactions

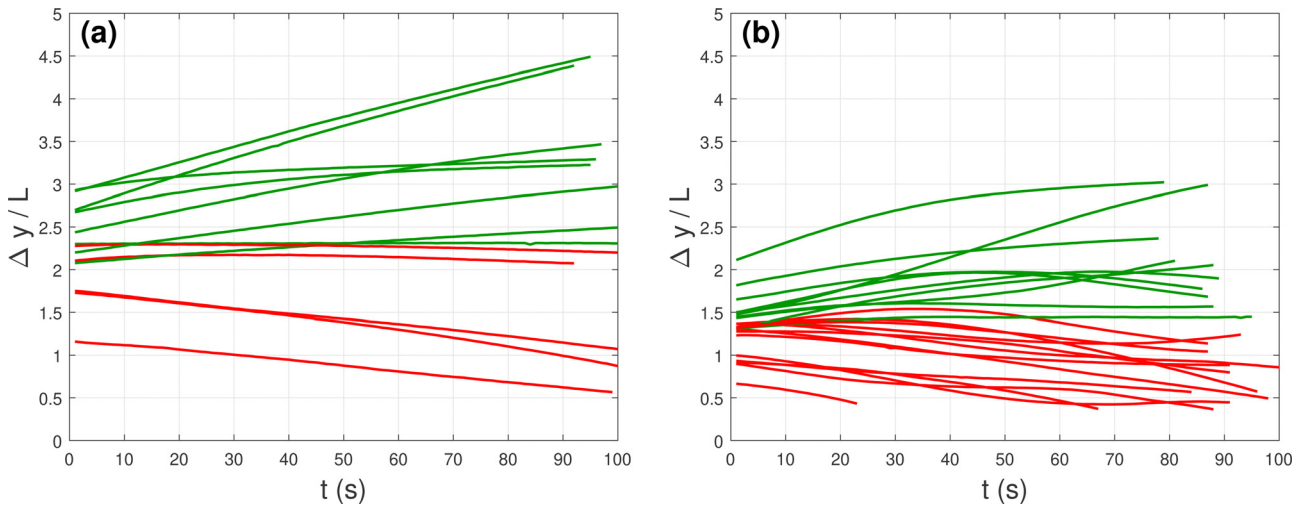

Fig. 9 The vertical distance between the ball chains, Δy, normalised with ball chain length L, as a function of time for (a) 12 beads and (b) 20 beads. The red curves represent ball chains that came closer to each other and the green ones – ball chains that moved away from each other.

between close filaments cause the lower one to be wider than the top one, as pointed out in ref. 14 and discussed in Section 5, in analogy to ref. 31. These shapes cause the lower ball chain to move slower than the upper one. It is clear that the closer the ball chains are to each other, the stronger they interact hydrodynamically.

On the other hand, the green curves in Fig. 9 correspond to two ball chains that are further from each other at the beginning of the run. Therefore, the influence of the isolated ball chain dynamics on their evolution is more pronounced. As discussed before, the time shift between the moments of the release of both 20-bead ball chains might explain why they move away from each other in the early stage of the runs. Indeed, as shown in Fig. 6(d), the velocity of an isolated ball chain increases with time in the early stage of its evolution. However, later it reaches a maximum and then decreases, which might be responsible for the non-monotonicity of some green curves in Fig. 9(b), showing that the ball chains initially move away from each other before eventually coming closer together. The dynamic changes of shapes for the 20-bead ball chains are also important. The 12-bead ball chains do not change their shapes so dynamically, which seems to be related to the almost monotonic curves in Fig. 9(a).

It might be interesting to compare the widths of the top and bottom ball chains, W_{top} and W_{bot}, as defined in Fig. 4(b). The ball chains in the current experiments exhibit significant out-of-plane motion, such as rotation and bending. It is thus challenging to determine the width of the ball chains since in general, they are not in a plane that would coincide with either plane of the camera views. However, there exist a few runs in which both ball chains do not exhibit significant rotation or out-of-plane bending. We measure the ball chain width W of such runs, but we only consider frames in which both top and bottom ball chains are planar, and their planes coincide with the perpendicular planes of the camera view. In other words, the top ball chain needs to stay within the plane of view of camera 1 and perpendicular to the plane of view of camera 2. At the same time, the bottom ball chain needs to stay within the plane of view of camera 2 and perpendicular to the plane of view of camera 1. Our analysis is thus reduced to only a few runs that satisfy these conditions.

In Fig. 10, we plot the difference in widths of the top and bottom ball chains, $W_{top} - W_{bot}$, normalised with the ball chain length L, as a function of the time t. It is evident from the plot that $W_{top} > W_{bot}$ for runs in which the ball chains move away from each other, and $W_{top} < W_{bot}$ for the runs in which the ball chains approach each other.

The small number of curves shown in Fig. 10 is related to a generic feature of the dynamics observed in our experiments: the ball chains tend to rotate and bend out of a plane. There are only 5 runs (out of 13) for 12-bead ball chains, and only 3 runs (out of 23) for 20-bead ball chains, such that both ball chain shapes remain in a single plane, and also only for a limited period of time at the early stage of the evolution, as shown in Fig. 10. Typically, the ball chains do not remain in their original planes. Our experiments indicate that the out-of-plane motion of very flexible elongated objects is ubiquitous and that their purely planar motion would seldom be observed in practical situations.

4 Numerical simulations of a single elastic fibre

In the experiments, the ball chains are flexible until a limit bending angle is reached. They are assumed to move and deform in a similar way to highly elastic fibres. To confirm this, we compare the experiments with numerical simulations of elastic fibres. Taking into account the sensitivity of the experimental results to the initial conditions, we focus our numerical analysis on a single sedimenting highly elastic fibre. The goal is to verify whether we can theoretically reproduce

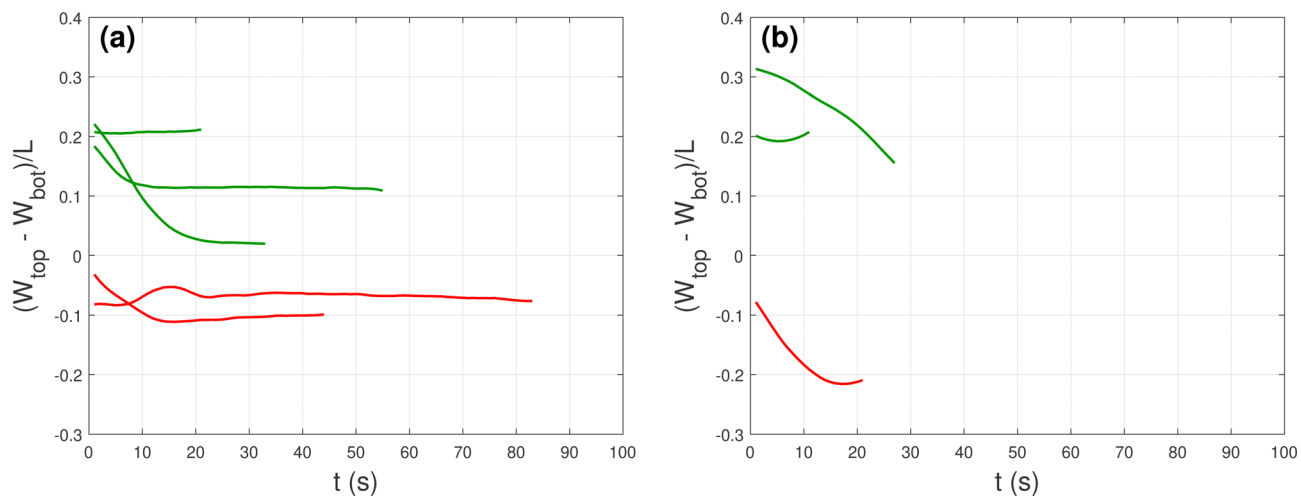

Fig. 10 Difference $(W_{top} - W_{bot})/L$ of the top and bottom ball chain widths as a function of time, for (a) 12 beads and (b) 20 beads. The red curves represent ball chains that came closer to each other, and the green ones represent ball chains that moved away from each other.

basic features of the dynamics observed in our experiments, *i.e.*, a non-stationary fibre shape which may exhibit rotation, out-of-plane deformation and which may have a non-horizontal end-to-end vector connecting the first and the last beads.

4.1 Theoretical description

In order to model the dynamics of a single fibre settling under gravity in a viscous fluid at a Reynolds number much smaller than unity, we employ the bead-chain model in which the fibre is represented by N identical spherical beads of a diameter d.[32] Centres of consecutive beads are connected by springs. The distance between the centres of the consecutive beads (the bond length) at the elastic equilibrium is l_0, chosen to be very close to the bead diameter, $l_0 = 1.01d$. Thus the length of the fibre at the elastic equilibrium is $L_0 = (N-1)\cdot l_0 + d$.

To represent almost inextensible elastic interactions between the consecutive beads i and $j = i+1$, with $i = 1,\ldots,N-1$, we employ finitely extensible nonlinear elastic (FENE) potential energy that has the following form:[33,34]

$$U^{\mathrm{FENE}} = -\frac{1}{2}k(l_0-d)^2\sum_{i=1}^{N-1}\ln\left[1-\left(\frac{r_{i,i+1}-l_0}{l_0-d}\right)^2\right]. \quad (2)$$

Here, $r_{i,j} = |\boldsymbol{r}_i - \boldsymbol{r}_j|$ is the distance between the centres of beads i and j (in particular, $r_{i,i+1}$ is the length of bond i), with $\boldsymbol{r}_i$ being a time-dependent position of bead i, and k is the spring constant.

With the FENE potential energy defined in eqn (2), the distance between surfaces of the consecutive beads, initially equal to $0.01d$, stays very small during settling, and does not exceed $0.02d$. For such a small gap, lubrication interactions with the fluid suppress spurious rotations of the beads.[35]

At the elastic equilibrium, the fibre is straight. During its settling, it resists deformations by bending forces between triplets of the consecutive beads. We employ the harmonic bending potential energy:[15,28,29,36,37]

$$U^{\mathrm{b}} = \frac{\mathscr{A}}{2l_0}\sum_{i=2}^{N-1}\beta_i^2. \quad (3)$$

Here, β_i is the bending angle of a triplet of consecutive beads $i-1, i, i+1$, defined in eqn (1) and shown in Fig. 3, and $\mathscr{A}$ is the bending stiffness. Based on the model of an elastic cylinder of diameter d,[38] the expressions

$$\begin{cases} k = E_{\mathrm{Y}}\pi d^2/(4l_0) \\ \mathscr{A} = E_{\mathrm{Y}}\pi d^4/64 \end{cases} \quad (4)$$

allow identification of the spring constant k and the bending stiffness $\mathscr{A}$ if the Young's modulus E_{Y} is known.[15]

The total elastic potential energy of the fibre has the form,

$$U = U^{\mathrm{FENE}} + U^{\mathrm{b}}. \quad (5)$$

The elastic force on a bead i is

$$\boldsymbol{F}_i^{\mathrm{e}} = -\frac{\partial}{\partial \boldsymbol{r}_i}U. \quad (6)$$

Summarising, we describe the elasticity of a fibre based on the model of an elastic cylinder of diameter d. In this model, there are strict relationships between the bending stiffness $\mathscr{A}$ and Young's modulus E_{Y}, and also between the spring constant k and E_{Y} (see eqn (4)). Hence, setting $\mathscr{A}$ to a very low number (but not zero) leads to a very small spring constant k. To keep the fibre almost inextensible, we employ a finitely extensible nonlinear elastic (FENE) potential (see eqn (2)). Hence, even in the case of a very small but finite spring constant, centres of two consecutive beads remain closer to each other than $1.02d$. In contrast, for $\mathscr{A} = 0$ and $k = 0$ the dynamics would be different. There would be no connections between consecutive beads. Fibre would not exist as a single object. The limit of zero bending is singular.

In addition to the elastic forces, each bead is subject to the same constant external gravitational force, $\boldsymbol{F}^g = -mg\cdot\hat{\mathbf{y}}$, where g is the gravitational acceleration, $\hat{\mathbf{y}}$ is the unit vector along the y axis, and m is the bead mass corrected for buoyancy. The total external force on bead i reads,

$$\boldsymbol{F}_i = \boldsymbol{F}_i^{\mathrm{e}} + \boldsymbol{F}^g. \quad (7)$$

Dimensionless elasto-gravitational number B estimates the ratio of gravitational to bending forces in the following way:[14,15,20,25,26,30]

$$B = L_0{}^2Nmg/\mathscr{A}, \quad (8)$$

with larger values of B corresponding to fibres that are more flexible.

As the Reynolds number in our experiments is very small, $\mathrm{Re} \ll 1$, we assume that the fluid flow satisfies the Stokes equations. We use the multipole expansion of solutions to the Stokes equations,[39,40] and assume stick boundary conditions on the surfaces of the beads. Then, we introduce the lubrication correction to speed up the convergence of the multipole expansion.[41,42] We apply the lubrication correction only to the relative motions, as described in ref. 42. In this paper, the order of the truncation of the multipole expansion is equal to 3. In Appendix A.1, we demonstrate a weak dependence of the dynamics of a single flexible fibre on a chosen order of truncation: 2, 3, or 4.

We obtain the following set of the first-order ODEs for the time-dependent positions $\boldsymbol{r}_i$ of the bead centres, $i = 1,\ldots,N$,

$$\dot{\boldsymbol{r}}_i = \sum_{j=1}^{N}\boldsymbol{\mu}_{ij}\cdot\boldsymbol{F}_j, \quad (9)$$

with the mobility matrices $\boldsymbol{\mu}_{ij}$ that depend on the positions of all the beads, and are evaluated from the multipole expansion by the precise numerical codes HYDROMULTIPOLE.[42,43]

The numerical codes HYDROMULTIPOLE are capable of evaluating the mobility matrices in the presence of interfaces.[44–49] However, here we applied the model of an infinite fluid since during the experimental observations the fibres were relatively far away from the container walls and the free surface.

Here we have used dimensionless variables, using as the length and time units d and $\tau_b = \frac{\pi\eta d^2}{mg}$, respectively, where η is the fluid dynamic viscosity. The velocity unit is $v_b = \frac{d}{\tau_b} = \frac{mg}{\pi\eta d}$.

4.2 Results: sedimentation of a single elastic fibre

Numerical simulations were performed of the dynamics of a single fibre having different numbers N of the beads. Here we present the results for either $N = 14$ (shorter fibre) or $N = 24$ (longer fibre). The aspect ratios of these fibres were chosen to be similar to the aspect ratios of the ball chains in our experiments.

Very flexible fibres were assumed in this study, with the elasto-gravitational number in the range $4000 < B < 10\,000$. The choice of a very large B was obvious to model very flexible ball chains in the experiment. The specific choice of values was guided by the requirement that the elasto-gravitational number is large enough to allow for excitation of higher bending modes, with out-of-plane deformations, and lack of stability of a U-shaped configuration, reported in ref. 14 and 20. This condition was needed to match our experimental observations.

Due to the experimental conditions, we are interested in relatively short times of the evolution that allow us to study only the initial stage of the settling dynamics. Before the beginning of the observations, while settling on the distance of 10 cm, *i.e.*, $67d$, the ball chains already reach U-shaped almost planar configurations. For very flexible elastic fibres the characteristic times to bend are also very short.[20] The height of the observed part of our glass tank is about 300 mm, *i.e.*, about $200d$, and therefore simulations cover about $300d$ in the vertical direction. This distance is reached at about $255\tau_b$ in the case of a shorter fibre with $N = 14$ beads, which is slower than about $235\tau_b$ required for a longer one with $N = 24$ beads. Nevertheless, in either case, this time is usually smaller than the time required to reach one of the stationary or stable periodic modes of sedimentation. Moreover, the time needed to destabilize U-shaped or W-shaped configurations is very sensitive to its out-of-plane perturbations.

Therefore, it is essential to choose appropriate initial conditions in the simulations, allowing for a fast destabilisation and triggering out-of-plane dynamics as early as possible rather than matching precisely the initial configurations observed in the experiments. It is known that an initially straight fibre, horizontal or inclined, does not destabilize quickly even if a small random perturbation is added,[14,20] as discussed in Appendix A.2. Taking this into account, we searched for initial configurations close to elastic equilibrium but not in a vertical plane. We used such configurations: an inclined planar C shape

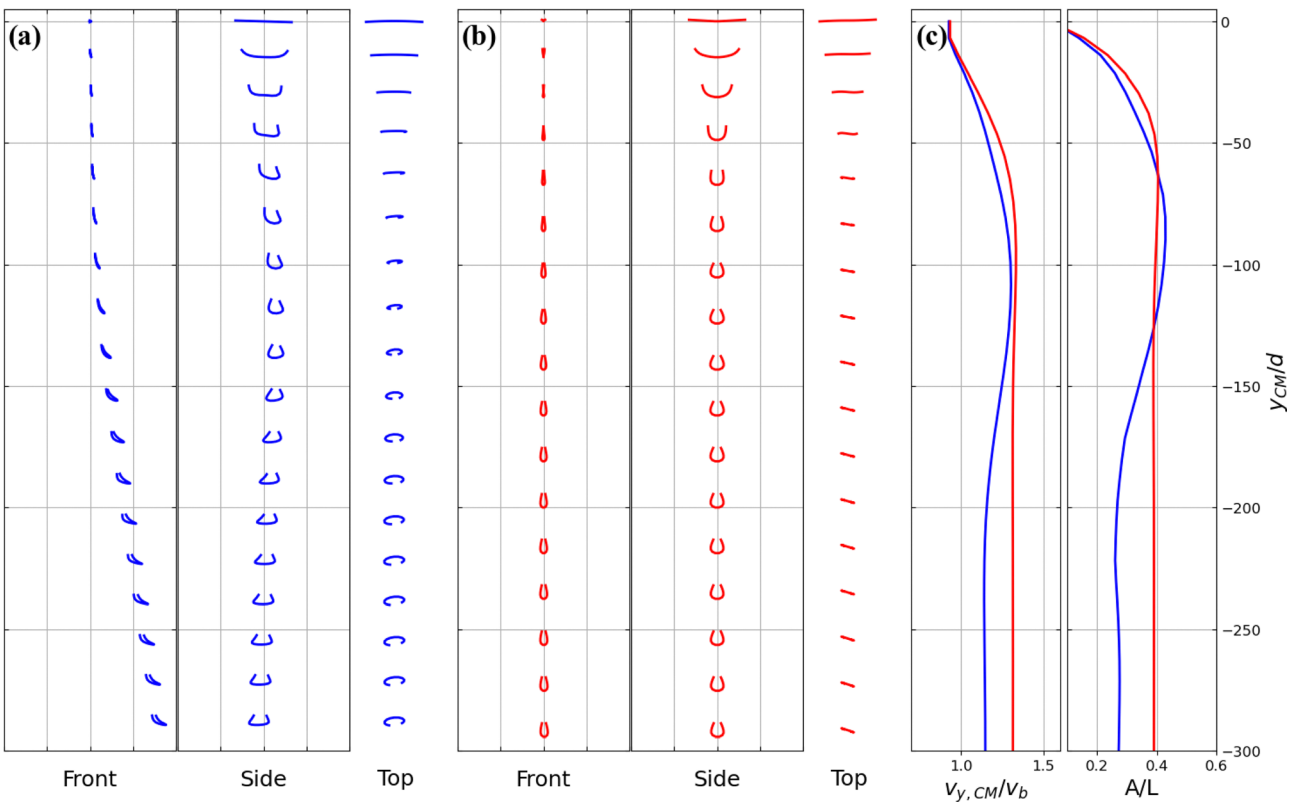

Fig. 11 Simulation results for a single elastic fibre made of 14 beads settling under gravity. (a and b) Snapshots taken at the time intervals $\Delta t = 14.5\tau_b$ for (a) $B = 8500$ and initially C-shape, and (b) $B = 8500$ and initially symmetric propeller shape. (c) The sedimentation velocity of the centre of mass $v_{y,CM}/v_b$ and the bending amplitude A/L *vs.* vertical component of the centre-of-mass position y_{CM}/d, plotted with blue and red lines for the cases shown in (a) and (b), respectively.

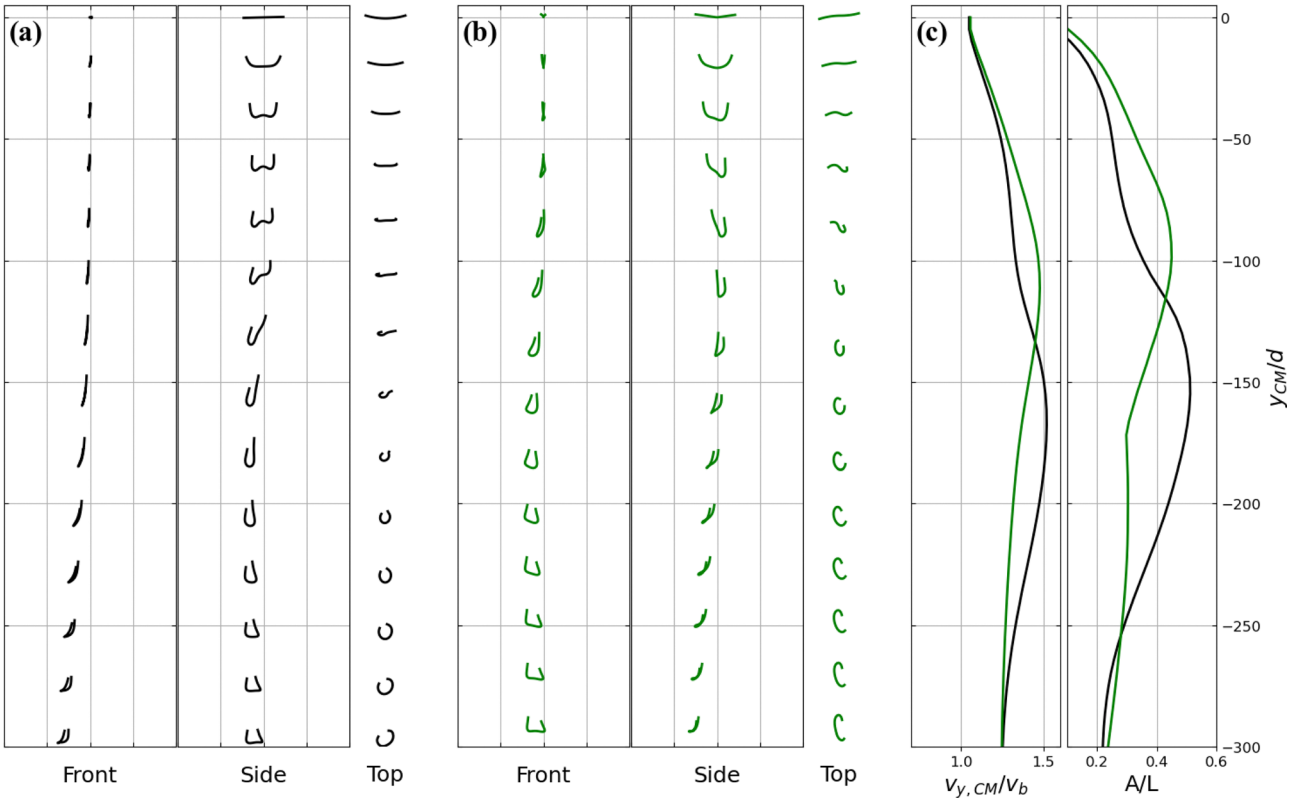

Fig. 12 Simulation results for a single elastic fibre made of 24 beads settling under gravity. (a and b) Snapshots taken at the time intervals $\Delta t = 17\tau_b$ for (a) $B = 8500$ and initially C-shape, and (b) $B = 8500$ and initially asymmetric propeller shape. (c) The sedimentation velocity of the centre of mass $v_{y,CM}/v_b$ and the bending amplitude A/L *vs.* vertical component of the centre-of-mass position y_{CM}/d, plotted with black and green lines for the cases shown in (a) and (b), respectively.

with a non-horizontal end-to-end vector (in short, C-shape), and a propeller shape, with horizontal and non-horizontal end-to-end vector (in short, symmetric and asymmetric propeller shapes, respectively). These three types of the initial configurations are specified in detail in Appendix A.3. The initial configurations are only slightly disturbed in comparison to a straight fibre in elastic equilibrium, as shown in the first snapshots in Fig. 11(a, b) and 12(a, b).

The elastic fibres made of 14 beads, shown in Fig. 11, rotate. This is a generic feature seen in our numerical simulations, in agreement with the experimental observations presented in Fig. 5(b and c) and the corresponding Videos 5b and c (ESI†). In the simulations, initial shapes with a slightly non-horizontal end-to-end position seem to have one arm higher than the other for a long time, also in agreement with the experiments, illustrated in Fig. 5. In addition, in the simulations such shapes significantly deform out of a vertical plane, as shown in Fig. 11(a).

Simulations of longer elastic fibres, made of 24 beads, also demonstrate an evolution pattern similar to that seen in the experiments (compare Fig. 12 to Fig. 6). The fibres form a W-shape, then tilt it and form a hook, and deform out of a vertical plane while decreasing the difference between vertical coordinates of the ends.

It is interesting to point out that the formation of the W-shape depends not only on the value of B,[14] but also on the fibre aspect ratio N. It does not take place for shorter fibres made up of 14 beads, while it is present for longer fibres made up of 24 beads, with the same value of the elasto-gravitational number B.

In connection with the experimental findings, it is worth investigating in the simulations if the initially imposed small left-right asymmetry of the fibre shape will decrease or increase with time, or oscillate or stabilize. To see it, we evaluate for each time the difference $\Delta A = y_N - y_1$ between vertical coordinate, y_N and y_1, of the positions of the centres of the last and the first bead of the fibre. Then, $\Delta A/d$ is plotted in Fig. 13(a) as a function of the dimensionless instantaneous vertical coordinate y_{CM}/d of the fibre centre of mass, for the numerical trials shown in Fig. 11 and 12, with the same colours. It is clear that the initially small (but non-zero) value of $\Delta A = y_N - y_1$ increases when the fibre settles down and then oscillates for quite a long time. Therefore, a non-horizontal end-to-end position seems to be an inherent feature of the fibre dynamics on a relatively short time scale, taking into account usually a random initial perturbation of the fibre shape.

To estimate the rotation along the y-axis, we proceed as follows. For each time, we evaluate the moment of inertia tensor and its eigenvectors and eigenvalues. The eigenvector corresponding to the largest eigenvalue determines a unit vector $\boldsymbol{n}$. Using spherical coordinates with vertical zenith

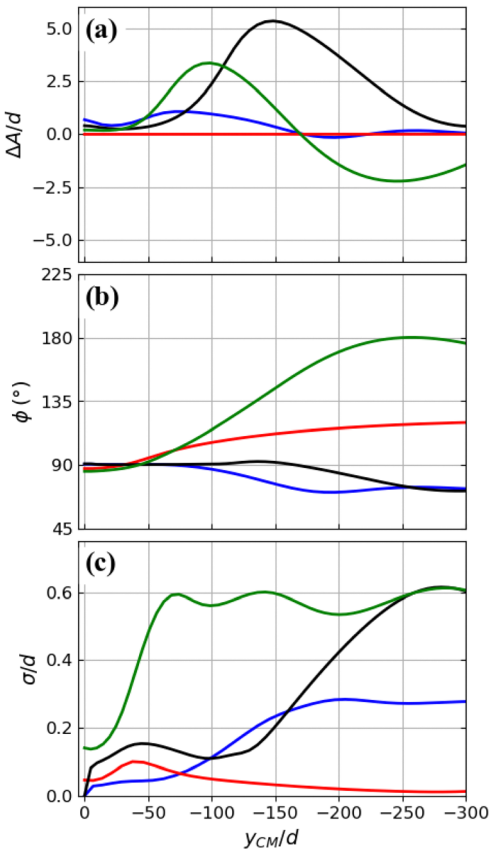

Fig. 13 (a) Difference $\Delta A/d$ between vertical positions of the fibre ends, (b) azimuthal angle ϕ and (c) non-flatness σ/d, plotted as functions of vertical component of the centre-of-mass position y_{CM}/d for the numerical trials shown in Fig. 11 and 12, with the same meaning of the colours.

direction, vector $\boldsymbol{n}$ can be determined by the polar angle θ it makes with the y-axis and the azimuthal angle ϕ that its horizontal projection makes with the x-axis. We evaluate ϕ for each time instant t and plot ϕ in Fig. 13b as a function of the dimensionless instantaneous vertical coordinate y_{CM}/d of the fibre centre of mass, for the numerical trials shown in Fig. 11 and 12, with the same meaning of the colours. It is clear that the polar angle ϕ changes significantly with time, also in agreement with the experiments. In the simulations, we observe that the changes of ϕ are often non-monotonic, what is related to shape deformations.

In the simulations, we observe that very flexible fibres typically tend to deform out of plane. To describe this feature quantitatively, we determine how far the shapes are from "an average" plane that contains the centre of mass of the fibre and is spanned by two eigenvectors that correspond to the smaller eigenvalues. In this plane the fibre would be positioned if its shape was flat. With this goal in mind, we evaluate the following time-dependent non-flatness parameter σ:

$$\sigma = \sqrt{\frac{1}{N}\sum_{i=1}^{N} h_i^2}, \qquad (10)$$

where h_i is the distance of the centre of bead i from the plane and the summation is over all the beads. Obviously, $\sigma = 0$ if the fibre is planar.

In Fig. 13(c), we plot σ/d *versus* the vertical position of the fibre centre-of-mass, and y_{CM}/d for the numerical trials shown in Fig. 11 and 12, with the same colours. As shown in Appendix A.4, all the considered highly elastic fibres, even if initially flat, after a certain time become non-planar as they settle down, and their non-flatness is pronounced.

Typical bending angles in the simulations are comparable with those observed in the experiments. The details are provided in Appendix A.5.

5 Theoretical remarks on the dynamics of two highly elastic filaments

In the limit of highly elastic fibres, with $B \gg 1$, gravitational forces dominate the elastic ones. Therefore, it might be useful to analyse a simple model of two pairs of identical point particles, (1,2) and (3,4), sedimenting down under identical gravitational forces without any other external forces. The configuration of the particles is shown in Fig. 14. The distance between particles 1 and 2 is the same as the distance between particles 3 and 4. Vertical planes determined by pairs (1,2) and (3,4) are perpendicular to each other. Each pair is oriented horizontally, but particles 1 and 2 are higher than particles 3 and 4. The centre of mass of particles 1 and 2 is located exactly above the centre of mass of particles 3 and 4.

In the point-particle model, the dynamics are governed by eqn (9) with the dimensionless mobility matrices, normalized by $(\pi\eta d)^{-1}$.

$$\boldsymbol{\mu}_{ij} = (\boldsymbol{I} + \hat{\boldsymbol{r}}_{ij}\hat{\boldsymbol{r}}_{ij})/(8r_{ij}) \quad \text{for} \quad i \neq j, \quad \boldsymbol{\mu}_{ii} = \boldsymbol{I}/3, \qquad (11)$$

where $\boldsymbol{r}_{ij} = \boldsymbol{r}_i - \boldsymbol{r}_j$, $r_{ij} = |\boldsymbol{r}_{ij}|$ and $\hat{\boldsymbol{r}}_{ij} = \boldsymbol{r}_{ij}/r_{ij}$. Positions $\boldsymbol{r}_i$ of the bead centers are normalised by d.

Hydrodynamic interactions between the point particles cause the upper particles 1 and 2 to approach each other, and the lower particles 3 and 4 to move away from each other,

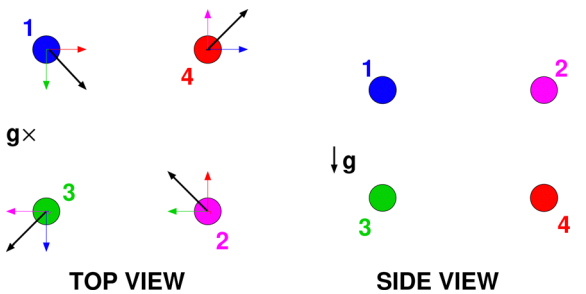

Fig. 14 A simplified model of two highly elastic fibres, represented as two pairs of identical point-particles, (1,2) and (3,4), sedimenting down in the gravitational field $\boldsymbol{g}$. The colour vectors indicate contributions to the horizontal velocity of a given particle, coming from another particle of this colour. The sums of these velocity contributions are marked as black vectors. It is clear that the upper particles approach each other, and the lower ones move away from each other.

as illustrated in Fig. 14. After these changes of the distances, the settling velocity of the upper particles will become greater than that of the lower particles, and both pairs will approach each other. This extremely simple model is in qualitative agreement with the attraction of close ball chains in our experiments.

It can be easily shown in a similar way that attraction of the upper point particles and repulsion of the lower point particles are also present if they are located in the same vertical plane, or if two vertical planes form an angle not equal to $\pi/2$. In the latter case, it can also be easily deduced that the whole system rotates. All these observations are in qualitative agreement with the dynamics of two elastic fibres, one above the other, discussed in ref. 14. A similar effect was reported in ref. 31. It was shown there that a single point particle above a cloud of point particles will cause the cloud to become wider and flatter.

Therefore, for our system of two flexible fibres, attraction is generic for initially similar shapes. On the other hand, differences in shapes can lead to repulsion.

6 Conclusions

In this paper, we investigated the dynamics of very flexible filaments sedimenting in a viscous fluid at a Reynolds number much smaller than unity. In the experimental study, we used ball chains and silicon oil. We also performed numerical simulation of the evolution of highly elastic fibres with the elasto-gravitational number $B > 4000$, using the precise HYDROMULTIPOLE numerical codes, based on the multipole expansion of the Stokes equations. We have demonstrated that the dynamics of ball chains and highly elastic filaments are similar to each other.

We observed that the dynamics of shorter and longer ball chains are different. In the early stage of the evolution, shorter ball chains form shapes that could be approximately classified as vertically oriented planar U-shapes while longer ball chains form shapes close to vertically oriented planar W-shapes. These findings agree with numerical studies of sedimenting elastic filaments carried out earlier,[14,20,27] and also in this paper. To the best of our knowledge, W-shapes of very flexible filaments have not been observed in experiments so far.

However, we observed that vertically oriented planar U- and W-shapes do not seem to be stable, unlike more stiff elastic filaments.[14,20–22,25] In the experiments, we found that shorter ball chains typically rotate; moreover, their end-to-end vectors are not horizontal and sometimes even increase the inclination angle with time. Longer ball chains relatively quickly deform significantly and move out of a vertical plane. These features are also present in our numerical simulations of highly elastic fibres with a large value of B, providing the choice of initially out-of-plane configurations with a non-horizontal end-to-end vector.

The experimental observations are limited to relatively short times, owing to the height of the container. Therefore, the numerical simulations presented here were also performed for a comparable range of times and vertical distances. The numerical study of the longtime behaviour of sedimenting highly elastic fibres will be the subject of a separate article, with an emphasis on the identification of attractors of the dynamics: periodic motions or stationary configurations. Those results would extend the class of the solutions shown in ref. 14.

Finally, in the experiments, we also studied hydrodynamic interactions between two ball chains, sedimenting one above the other, initially in approximately perpendicular vertical planes. We have shown that, depending on the initial conditions and length, they can approach each other (so-called attraction) or move away from each other (so-called repulsion). In previous studies, the attraction of elastic fibres at symmetric initial configurations one above the other has been found numerically,[14,30] but not the repulsion: our results are new.

In the literature, two highly elastic fibres with large values of B have been observed numerically to always move away from each other if initially straight and in the same horizontal plane: collinear[30] or in a symmetric configuration.[26] For moderate values of B and the symmetric initial configurations of two elastic fibres, an attracting stationary relative configuration has been found, with attraction at larger distances and repulsion at smaller ones.[26,50] The examples discussed above illustrate the complexity of the sedimentation of multiple flexible objects. This work is just a step towards understanding its basic features.

Conflicts of interest

There are no conflicts to declare.

Appendices

A Details of the numerical simulations

A.1 Multipole truncation order L

The dependence of the results on the multipole truncation order L was tested for $L = 2, 3, 4$. It was found that differences between the results of the simulations for $L = 2$ and $L = 3$ are very small, and sequences of shapes look almost the same. The difference between the results for $L = 3$ and $L = 4$ is even much smaller, practically negligible, in agreement with the previous analysis of the accuracy of the multipole expansion corrected for lubrication.[40,42] As an example, the green curves ($N = 24$, $B = 8500$, initially asymmetric propeller shape) from Fig. 13, obtained for $L = 3$, are in Fig. 15 compared with the curves for $L = 2$ and for $L = 4$. The curves for $L = 4$ and for $L = 3$ are superimposed.

A.2 Straight fibres with a very small random perturbation and their evolution

It is known from the literature[14,20] that it takes a lot of time to observe an out-of-plane instability of a highly elastic, almost

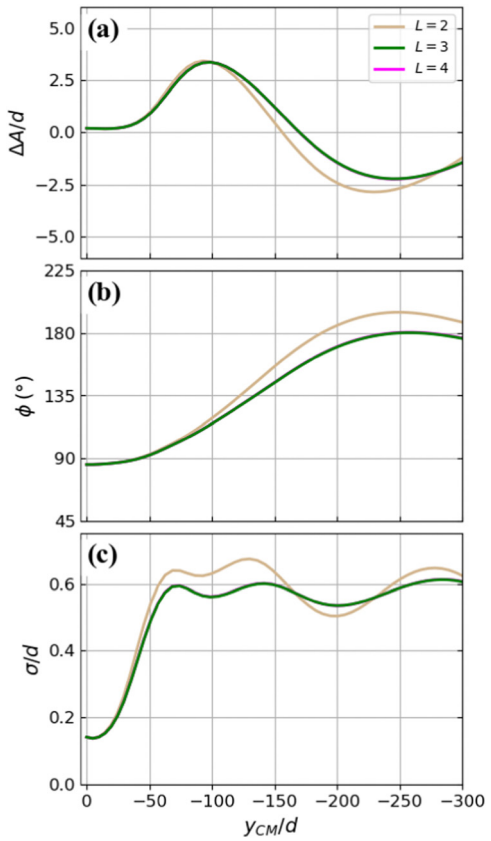

Fig. 15 Sensitivity of the numerical results to the multipole truncation order L for $N = 24$, $B = 8500$ and initially asymmetric propeller shape. (a) Difference $\Delta A/d$ between vertical positions of the fibre ends, (b) azimuthal angle ϕ and (c) non-flatness σ/d, plotted as functions of the vertical component of the centre-of-mass position y_{CM}/d. The magenta curve ($L = 4$) is under the green curve ($L = 3$).

straight fibre, and in this Appendix, we provide some estimations of how fast it grows.

Assume that a straight elastic fibre at the elastic equilibrium is oriented horizontally or inclined at a certain angle γ with respect to the horizontal plane, and perturb randomly positions of all the beads with a maximum amplitude $0.0001d$. Examples of the fibre dynamics for such initial configurations are described below.

Let us start with a short fibre with $N = 14$ beads. In the case of almost straight initial configurations, when the fibre is oriented horizontally, the fibre stays almost in a vertical plane and almost symmetric with respect to reflections in the perpendicular vertical plane for a relatively long time. The initial straight shape is turned into a U-shape relatively quickly but then the fibre keeps this shape for a long time. Only after that, the fibre stops sedimenting vertically only and starts moving also sideways. For example, in the case of a relatively flexible fibre with the elasto-gravitational number $B = 8000$, vertical sedimentation is observed until about $230\tau_b$ with the fibre travelling to a depth of about $290d$. Then symmetry of the U-shape remains to be present but the fibre starts drifting sideways similar to the intermediate mode reported in ref. 14. The results of simulations for such initial conditions cannot qualitatively describe the experimental results presented in Fig. 5. The initial inclination of the almost straight fibre does not lead to a rotation (a feature seen in the experimental trial (b) in Fig. 5) as the left-right symmetry of the U-shape is quickly restored. A non-horizontal orientation of the end-to-end vector seen in trial (c) in Fig. 5, does not occur in the simulations under these initial configurations either.

A similar situation is observed for a longer fibre with $N = 24$ beads in an almost straight initial configuration. For example, for $B = 8000$, the initial straight and horizontal shape is turned into a W-shape already at $18\tau_b$ at a depth of $20d$. It then retains an almost symmetric W-shape until $190\tau_b$ at $215d$ depth. Then it turns into a hook-shape preserved until the depth of $522d$ at $380\tau_b$. Nevertheless, the fibre is still oriented 'almost' vertically all this time: the polar angle θ for unit vector $\mathbf{n}$ starts to differ from 90° at $\approx 200\tau_b$ but decreases only to 89.7° at $380\tau_b$. This is similar to the initial stage of the sedimentation process presented in ref. 14 in the case of larger values of B. Similar to the case of a short fibre, the results of simulations for almost straight configurations of longer fibres cannot qualitatively describe features seen in the experimental results presented in Fig. 6. In brief, the evolution of tiny perturbations is too slow. We expect that in the experiment, perturbations are not tiny and not as random as, *e.g.*, in the Brownian motion.

Therefore, in this work, we used different initial configurations, with a small (but not tiny) perturbation from a vertical plane. Details will be given in the next section.

A.3 C-shaped and propeller-shaped initial configurations

Ultimately, we performed simulations for two families of initial configurations of fibres, described below.

(I) The fibre has a planar C-shape constructed in three steps:

(1) Shape of a circular arc, *i.e.* C-planar shape, is created using the following equations,

$$\begin{cases} x_i = r \cdot \sin\left(\left(i - \dfrac{N+1}{2}\right)\alpha\right) \\ y_i = 0 \\ z_i = r \cdot \cos\left(\left(i - \dfrac{N+1}{2}\right)\alpha\right) - r, \end{cases} \tag{12}$$

where α is the curvature angle, $r = l_0/(2\cdot\sin(\alpha/2))$ is the radius of the circular arc, and $\boldsymbol{r}_i = (x_i, y_i, z_i)$.

(2) The whole fibre is then inclined out of the horizontal plane by a certain tilt angle γ, *via* the rotation matrix

$$\mathscr{R} = \begin{bmatrix} \cos\gamma & -\sin\gamma & 0 \\ \sin\gamma & \cos\gamma & 0 \\ 0 & 0 & 1 \end{bmatrix}. \tag{13}$$

(3) Positions of all the beads are randomly disturbed with a maximum amplitude of $0.0001d$.

(II) The fibre has a propeller shape constructed in five steps:

(1) S-planar shape is created using eqn (14);

$$\begin{cases} x_i = r \cdot \sin\left(\left(i - \dfrac{2J+1}{2}\right)\alpha\right) \\ y_i = 0 \\ z_i = \pm\left(r \cdot \cos\left(\left(i - \dfrac{2J+1}{2}\right)\alpha\right) - r\right). \end{cases} \quad (14)$$

Here, sign "minus" is taken for the bead number i with $i \leq J$ and sign "plus" is taken for other beads.

(2) A specific bead J is chosen that, together with the neighbouring bead $(J+1)$ in case of an even N, will initially serve as a tip of the propeller.

(3) One arm of the fibre formed by the beads with $i \leq J$ is then inclined at a certain angle γ.

(4) Another arm of the fibre formed by the beads with $i \geq J+1$ is inclined at the angle $-\gamma$.

(5) Positions of beads are randomly disturbed with a maximum amplitude of $0.0001d$.

As the initial conditions in the simulations shown in Fig. 11, we took shapes with the following values of the parameters:

- C-shape with $\alpha = 1^\circ$ and $\gamma = 1^\circ$,
- Symmetric propeller shape with equal arms ($J = N/2$), $\alpha = 1^\circ$ and $\gamma = 5.65^\circ$.

As the initial conditions in the simulations shown in Fig. 12, we took shapes with the following values of the parameters:

- C-shape with $\alpha = 1^\circ$ and $\gamma = 1^\circ$,
- Asymmetric propeller shape with unequal arms ($J = N/2 - 1$), $\alpha = 1^\circ$ and $\gamma = 5.65^\circ$.

In Fig. 11(a, b) and 12(a, b), the first rows of the snapshots show the projections of the initial shapes defined above.

A.4 Non-flatness of an elastic fibre

All the considered highly elastic fibres, even if initially flat, after a certain time become significantly non-planar as they settle down. Their non-flatness is pronounced, as shown in Fig. 13(c) for all the initial configurations except the symmetric propeller shape (red curve). In Fig. 16 we illustrate that this red curve also increases, but later, for a larger settling distance.

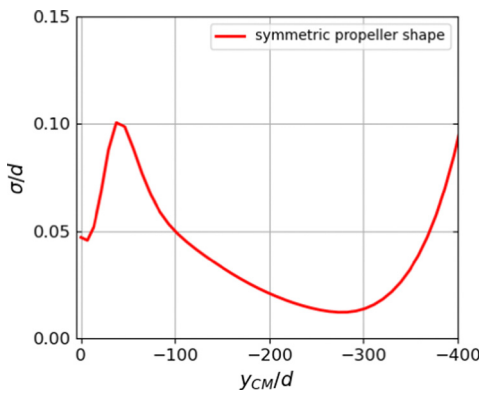

Fig. 16 Non-flatness σ/d plotted as a function of vertical component of the centre-of-mass position y_{CM}/d for the case with $N = 14$, $B = 8500$, and with a symmetric propeller shape as the initial configuration.

A.5 Evolution of the maximum bending angle of an elastic fibre

In the experiments, the ball chain local bending angles β_i typically did not exceed 33°–40°, being smaller than the maximum bending angle out of the fluid (around 55°). In the numerical simulations of flexible fibres, the maximum bending angles were typically of a comparable magnitude as in the experiments.

In the simulations of a short fibre with $N = 14$ beads, for the blue case, the bending angle starts with 1° at $y_{CM} = 0d$, then the maximum bending angle of 50° is achieved at depths of $y_{CM} \approx 50d$, and further down at $y_{CM} = 300d$ it decreases to 33°. For the red case, the bending angle starts with 6° at $y_{CM} = 0d$, then the maximum bending angle of 44° is achieved at depths of $y_{CM} \approx 70d$, and further down at $y_{CM} = 300d$ it decreases to 37°.

In the simulations of a long fibre with $N = 24$ beads, for the black case, the bending angle starts with 1° at $y_{CM} = 0d$, then the maximum bending angle of 39° is achieved at depths of $y_{CM} \approx 110d$, and further down at $y_{CM} = 300d$ it decreases to 24°. For the green case, the bending angle starts with 6° at $y_{CM} = 0d$, then the maximum bending angle of 35° is achieved at depths of $y_{CM} \approx 70d$, and further down at $y_{CM} = 300d$ it decreases to 28°.

B Experiment: description of the videos

A list of the experimental videos that are available in the ESI.† The names of the video files refer to the appropriate figure numbers.

Video 5a: settling of a single 12-bead ball chain under gravity in silicon oil recorded from two cameras with perpendicular lines of sight. Snapshots from this trial are shown in Fig. 5(a). The duration of the experiment in real-time is 132 s.

Video 5b: settling of a single 12-bead ball chain under gravity in silicon oil recorded from two cameras with perpendicular lines of sight. Snapshots from this trial are shown in Fig. 5(b). The ball chain rotates. The duration of the experiment in real-time is 128 s.

Video 5c: settling of a single 12-bead ball chain under gravity in silicon oil recorded from two cameras with perpendicular lines of sight. Snapshots from this trial are shown in Fig. 5(c). Rotation and non-horizontal orientation of the end-to-end vector are visible. The duration of the experiment in real-time is 136 s.

Video 6a: settling of a single 20-bead ball chain under gravity in silicon oil recorded from two cameras with perpendicular lines of sight. Snapshots from this trial are shown in Fig. 6(a). Formation of a W-shape in the early stage of the evolution is visible. The duration of the experiment in real-time is 110 s.

Video 6b: settling of a single 20-bead ball chain under gravity in silicon oil recorded from two cameras with perpendicular lines of sight. Snapshots from this trial are shown in Fig. 6(b). Formation of a wide, irregular U-shape in the early

stage of the evolution is visible. The duration of the experiment in real-time is 110 s.

Video 6c: settling of a single 20-bead ball chain under gravity in silicon oil recorded from two cameras with perpendicular lines of sight. Snapshots from this trial are shown in Fig. 6(c). A hook-shape is formed very early. The duration of the experiment in real-time is 110 s.

Video 7a: settling of a pair of 12-bead ball chains under gravity in silicon oil recorded from two cameras with perpendicular lines of sight. The ball chains were placed initially one above the other in perpendicular orientations. Snapshots from this trial are shown in Fig. 7(a). The ball chains approach each other. The duration of the experiment in real-time is 104 s.

Video 7c: settling of a pair of 12-bead ball chains under gravity in silicon oil recorded from two cameras with perpendicular lines of sight. The ball chains were placed initially one above the other in perpendicular orientations. Snapshots from this trial are shown in Fig. 7(c). The ball chains move away from each other. The duration of the experiment in real-time is 108 s.

Video 8a: settling of a pair of 20-bead ball chains under gravity in silicon oil recorded from two cameras with perpendicular lines of sight. The ball chains were placed initially one above the other in perpendicular orientations. Snapshots from this trial are shown in Fig. 8(a). The ball chains approach each other. The duration of the experiment in real-time is 108 s.

Video 8c: settling of a pair of 20-bead ball chains under gravity in silicon oil recorded from two cameras with perpendicular lines of sight. The ball chains were placed initially one above the other in perpendicular orientations. Snapshots from this trial are shown in Fig. 8(c). The ball chains move away from each other. The duration of the experiment in real-time is 140 s.

Acknowledgements

We thank Prof. Piotr Korczyk for providing us with Fig. 2. This work was supported in part by the National Science Centre under grant UMO-2018/31/B/ST8/03640.

Notes and references

1 T. A. Witten and H. Diamant, *Rep. Prog. Phys.*, 2020, **83**, 116601.
2 O. Du Roure, A. Lindner, E. N. Nazockdast and M. J. Shelley, *Annu. Rev. Fluid Mech.*, 2019, **51**, 539–572.
3 A. Lindner and M. J. Shelley, in *Fluid-Structure Interactions in Low Reynolds Number Flows*, ed. C. Duprat and H. A. Stone, Royal Society of Chemistry, 2015, pp. 168–189.
4 H. Nguyen and L. Fauci, *J. R. Soc., Interface*, 2014, **11**, 20140314.
5 V. Kantsler and R. E. Goldstein, *Phys. Rev. Lett.*, 2012, **108**, 038103.
6 M. Harasim, B. Wunderlich, O. Peleg, M. Kröger and A. R. Bausch, *Phys. Rev. Lett.*, 2013, **110**, 108302.
7 Y. Liu, B. Chakrabarti, D. Saintillan, A. Lindner and O. Du Roure, *Proc. Natl. Acad. Sci. U. S. A.*, 2018, **115**, 9438–9443.
8 X. Zhang, C. Caruso, W. A. Lam and M. D. Graham, *Phys. Rev. Fluids*, 2020, **5**, 053101.
9 J. K. Nunes, H. Constantin and H. A. Stone, *Soft Matter*, 2013, **9**, 4227–4235.
10 A. Perazzo, J. K. Nunes, S. Guido and H. A. Stone, *Proc. Natl. Acad. Sci. U. S. A.*, 2017, **114**, E8557–E8564.
11 J. Słomka, U. Alcolombri, E. Secchi, R. Stocker and V. I. Fernandez, *New J. Phys.*, 2020, **22**, 043016.
12 M. S. Rizvi, P. Peyla, A. Farutin and C. Misbah, *Phys. Rev. Fluids*, 2020, **5**, 033101.
13 N. Xue, J. K. Nunes and H. A. Stone, *Soft Matter*, 2022, **18**, 514–525.
14 G. Saggiorato, J. Elgeti, R. G. Winkler and G. Gompper, *Soft Matter*, 2015, **11**, 7337–7344.
15 M. Bukowicki and M. L. Ekiel-Jeżewska, *Soft Matter*, 2018, **14**, 5786–5799.
16 Y. Yu and M. D. Graham, *Soft Matter*, 2021, **17**, 543–553.
17 K. S. Silmore, M. S. Strano and J. W. Swan, *Soft Matter*, 2021, **17**, 4707–4718.
18 S. Ravichandran and J. Wettlaufer, *arXiv*, 2022, preprint, arXiv:2212.12014, DOI: **10.48550/arXiv.2212.12014**.
19 X. Xu and A. Nadim, *Phys. Rev. Fluids*, 1994, **6**, 2889–2893.
20 M. C. Lagomarsino, I. Pagonabarraga and C. P. Lowe, *Phys. Rev. Lett.*, 2005, **94**, 148104.
21 X. Schlagberger and R. R. Netz, *EPL*, 2005, **70**, 129.
22 M. Manghi, X. Schlagberger, Y.-W. Kim and R. R. Netz, *Soft Matter*, 2006, **2**, 653–668.
23 L. Li, H. Manikantan, D. Saintillan and S. E. Spagnolie, *J. Fluid Mech.*, 2013, **735**, 705–736.
24 B. Shojaei and H. Dehghani, *Indian J. Sci. Technol.*, 2015, **8**, 1.
25 B. Marchetti, V. Raspa, A. Lindner, O. Du Roure, L. Bergougnoux, E. Guazzelli and C. Duprat, *Phys. Rev. Fluids*, 2018, **3**, 104102.
26 M. Bukowicki and M. L. Ekiel-Jeżewska, *Soft Matter*, 2019, **15**, 9405–9417.
27 A. Koshakji, G. Chomette, J. Turner, J. Jablonski, A. Haynes, D. Carlucci, B. Giovanardi and R. A. Radovitzky, *J. Comput. Phys.*, 2023, **474**, 111774.
28 M. Gruziel, K. Thyagarajan, G. Dietler, A. Stasiak, M. L. Ekiel-Jeżewska and P. Szymczak, *Phys. Rev. Lett.*, 2018, **121**, 127801.
29 M. Gruziel-Słomka, P. Kondratiuk, P. Szymczak and M. L. Ekiel-Jeżewska, *Soft Matter*, 2019, **15**, 7262–7274.
30 I. Llopis, I. Pagonabarraga, M. C. Lagomarsino and C. P. Lowe, *Phys. Rev. E: Stat., Nonlinear, Soft Matter Phys.*, 2007, **76**, 061901.
31 M. L. Ekiel-Jeżewska, *Phys. Rev. E: Stat., Nonlinear, Soft Matter Phys.*, 2014, **90**, 043007.
32 E. Gauger and H. Stark, *Phys. Rev. E: Stat., Nonlinear, Soft Matter Phys.*, 2006, **74**, 021907.
33 H. R. Warner, *Ind. Eng. Chem. Fundam.*, 1972, **11**, 379–387.
34 R. Bird, R. C. Armstrong and O. Hassager, *Dynamics of Polymeric Liquids. Volume 1. Fluid Mechanics*, Wiley, New York, 1977.
35 A. M. Słowicka, E. Wajnryb and M. L. Ekiel-Jeżewska, *J. Chem. Phys.*, 2015, **143**, 124904.

36 C. Storm and P. C. Nelson, *Phys. Rev. E: Stat., Nonlinear, Soft Matter Phys.*, 2003, **67**, 051906.
37 Y. Li and M. Kröger, *Soft Matter*, 2012, **8**, 7822–7830.
38 L. D. Landau, E. M. Lifshitz, L. P. Pitaevskii and A. M. Kosevich, *Course of Theoretical Physics: Volume 7, Theory of Elasticity*, Butterworth-Heinemann, 1986.
39 S. Kim and S. Karrila, *Microhydrodynamics*, Heinemann, Boston, 1991.
40 B. Cichocki, B. U. Felderhof, K. Hinsen, E. Wajnryb and J. Bławzdziewicz, *J. Chem. Phys.*, 1994, **100**, 3780–3790.
41 L. Durlofsky, J. F. Brady and G. Bossis, *J. Fluid Mech.*, 1987, **180**, 21–49.
42 B. Cichocki, M. L. Ekiel-Jeżewska and E. Wajnryb, *J. Chem. Phys.*, 1999, **111**, 3265–3273.
43 M. L. Ekiel-Jeżewska and E. Wajnryb, in *Theoretical Methods for Micro Scale Viscous Flows*, ed. F. Feuillebois and A. Sellier, Transworld Research Network, Kerala, India, 1st edn, 2009, pp. 127–172.
44 B. Cichocki, R. B. Jones, R. Kutteh and E. Wajnryb, *J. Chem. Phys.*, 2000, **112**, 2548–2561.
45 B. Cichocki, M. L. Ekiel-Jeżewska, G. Nägele and E. Wajnryb, *J. Chem. Phys.*, 2004, **121**, 2305–2316.
46 B. Cichocki, M. L. Ekiel-Jeżewska and E. Wajnryb, *J. Chem. Phys.*, 2007, **126**, 184704.
47 S. Bhattacharya, J. Bławzdziewicz and E. Wajnryb, *Phys. A*, 2005, **356**, 294–340.
48 S. Bhattacharya, J. Bławzdziewicz and E. Wajnryb, *J. Fluid Mech.*, 2005, **541**, 263–292.
49 J. Bławzdziewicz, M. Ekiel-Jeżewska and E. Wajnryb, *J. Chem. Phys.*, 2010, **133**, 114702.
50 M. Bukowicki, M. Gruca and M. L. Ekiel-Jeżewska, *J. Fluid Mech.*, 2015, **767**, 95–108.

